· Article · **Advances in Polar Science**
doi: 10.13679/j.advps.2021.0021 June 2021 Vol. 32 No. 2: 105-117

Retrievals of Arctic sea ice melt pond depth and underlying ice thickness using optical data

ZHANG Hang, YU Miao, LU Peng*, ZHOU Jiaru & LI Zhijun

State Key Laboratory of Coastal and Offshore Engineering, Dalian University of Technology, Dalian 116024, China

Received on 6 May 2021; accepted on 17 June 2021; published online 30 June 2021

Abstract Melt pond is a distinctive characteristic of the summer Arctic, which affects energy balance in the Arctic system. The Delta-Eddington model (BL) and Two-strEam rAdiative transfer model (TEA) are employed to retrieving pond depth H_p and underlying ice thickness H_i according to the ratio X of the melt-pond albedo in two bands. Results showed that when $\lambda_1 = 359$ nm and $\lambda_2 = 605$ nm, the Pearson's correlation coefficient r between X and H_p is 0.99 for the BL model. The result of TEA model was similar to the BL model. The retrievals of H_p for the two models agreed well with field observations. For H_i, the highest r (0.99) was obtained when $\lambda_1 = 447$ nm and $\lambda_2 = 470$ nm for the BL model, $\lambda_1 = 447$ nm and $\lambda_2 = 451$ nm for the TEA model. Furthermore, the BL model was more suitable for the retrieval of thick ice ($0 < H_i < 3.5$ m, $R^2 = 0.632$), while the TEA model is on the contrary ($H_i < 1$ m, $R^2 = 0.842$). The present results provide a potential method for the remote sensing on melt pond and ice in the Arctic summer.

Keywords **Arctic, melt pond, sea ice, remote sensing, albedo**

Citation: Zhang H, Yu M, Lu P, et al. Retrievals of Arctic sea ice melt pond depth and underlying ice thickness using optical data. Adv Polar Sci, 2021, 32(2): 105-117, doi: 10.13679/j.advps.2021.0021

1 Introduction

Sea ice is the most important feature covering the ocean surface in the Arctic (Perovich et al., 2003). It can prevent direct heat exchange between the atmosphere and the ocean under sea ice by reflecting incident solar radiation, and plays an important role in regulating changes in the global climate and natural environment (Lenton, 2012; Qin et al., 2014).

In recent years, many studies have shown that Arctic summer sea ice is rapidly declining, not only in extent and area (Strove et al., 2007), but also in thickness. This is clear, especially in the later period of melting, which involves shrinking and thinning (Kwok and Rothrock, 2009). After Arctic sea ice begins to melt, melt-water from sea ice and snow accumulates in depressions of the sea-ice surface to form melt ponds. From June to September, the seasonal evolution of melt ponds can be observed to fall into five stages: pond formation, pond drainage, pond evolution, open water, and fall freeze-up. Before the pond refreezes, the pond depth increases gradually, and the underlying ice thickness decreases simultaneously (Polashenski et al., 2012; Lu et al., 2018a). This results in more solar radiation being absorbed by the sea ice and the underlying ocean due to the gradually decreasing broadband albedo, further promoting the melting of sea ice (Katlein et al., 2015; Perovich et al., 2002a).

Melt ponds play an increasingly important role in the melting of Arctic sea ice. Specifically, the depth of the melt pond is an important parameter. As melt pond depth increases, the surface broadband albedo of the melt pond decreases rapidly, especially in the initial stage of melt pond formation (Makashtas and Podgorny, 1996; Lu et al., 2016). Moreover, melt ponds have a significant energy absorption capacity, which greatly affects the partitioning of solar energy within the atmosphere, melt pond, underlying sea ice, and the ocean beneath the ice. As the depth of the melt pond

---

[*] Corresponding author, ORCID: 0000-0002-4366-8807, E-mail: lupeng@dlut.edu.cn

increases, the energy absorbed by the melt pond becomes significantly greater than the energy absorbed by the underlying ice and ocean under the ice (Lu et al., 2018b). Melt ponds also affect the desalination process of sea ice. The coalesced brine channels due to the increasing porosities during melting give rise to downward flushing of surface meltwater into the ocean due to gravity and reduce the salinity of Arctic summer sea ice (Notz and Worster, 2009). In recent years, more and more numerical simulations have been incorporated into explicit melt pond models or parameterizations to consider the effects of melt ponds. Skyllingstad et al. (2009) described the growing process of melt ponds on permeable sea ice in the Arctic and found that the melting rate of the sidewalls of the melt pond was greater than that of the underlying ice. The model of Popović and Abbot (2017) considered melt pond growth caused by vertical melting of the sea ice bottom. They found that the melt pond growth rate was more sensitive to changes in bare sea-ice albedo than changes in pond albedo unless the ice was already mostly covered in ponds. Lu et al. (2016) used a Two-strEam rAdiative transfer model (TEA) and found that the surface albedo of a melt pond was mainly dependent on pond depth H_p and underlying ice thickness H_i.

However, due to the severe weather conditions and marine environment in the Arctic region, existing observations of melt ponds mainly focus on the horizontal scale, such as coverage and size (Perovich et al., 2002b; Li et al., 2017; Wang et al., 2020). Whereas, few studies have recorded the depth evolution process of a melt pond (Scott and Feltham, 2010; Tsamados et al., 2015). The main reason for this is that melt ponds are relatively shallow, and their depth is difficult to determine by satellite remote sensing. In addition, changes in H_p are related to H_i (Holland et al., 2006), and the remote sensing data of the Arctic summer sea ice thickness has always been gaped (Ji, 2015). The ICESat and Cryosat-2 satellites only provide sea ice thickness data in the period from October to April of the next year. The reason is closely related to the accuracy of leads identifying, the algorithm model parameters (snow thickness and density, sea ice and ocean density) and the uncertainty of microwave or laser penetration depth in the melting ice (Kwok and Cunningham, 2008; Ji et al., 2015). ICESat-2 is capable to distinguish between leads and ponds. Farrel et al. (2020) showed the potential of ICESat-2 for H_p retrieval.

To make up for the lack of existing sea-ice remote-sensing products in summer and to provide strong data support for simulating and verifying rapid changes in melt ponds and sea ice, this paper explores the possibility of using the reflection characteristics of summer sea ice to retrieve H_p and H_i based on four methods (Legleiter et al., 2014; Lu et al., 2018a; Malinka et al., 2018; König and Oppelt, 2020). The four existing methods are introduced in Section 2. Improvement to the method proposed by Legleiter et al. (2014) and validation using field measurement are presented in Section 3. The influence of sky conditions is discussed in Section 4. Conclusions are finally drawn in Section 5.

2 Retrieval methods of H_p and H_i

2.1 Summary of previous retrieval methods

Table 1 summarizes the major methods proposed in recent years for retrieving H_p and H_i according to optical properties. Also shown are the main ideas and the calculation processes of each method.

Table 1 Summary of the retrieval methods for H_p and H_i

Reference	Ice type	Input parameters	Output parameters and the range used for verification	Accuracies	Advantage	Notes	Illumination condition	Instrument setups
Legleiter et al., 2014	Glacier ice	Melt pond spectral reflectance	H_p (H_p: 0.31–10.45 m)	R^2=0.93 ε=0.65 m (n=4398)	This study demonstrated the feasibility of use WV2 to retrieve H_p on the Greenland ice sheet. The deeper the pond depth, the better the retrieval effect.	This method did not establish a general relation between H_p and reflectance	Good atmospheric conditions	Spectrometers
Lu et al., 2018a	Sea ice	Melt pond color (RGB or HSL intensity)	H_i and H_p (H_i<1 m)	H_p: R^2=0.671 ε=0.156 m (n=5)	The color of melt ponds is easy to measure, the retrieval effect of thin ice is better (H_i<1 m)	The relationship between simulated and measured H_p is not apparent.	Overcast sky condition	Digital camera
Malinka et al., 2018	Sea ice	Melt pond surface spectral albedo	H_i, H_p, and σ_t (H_p: 0–0.5 m H_i: 0–3 m)	H_i: R^2=0.56 ε=0.215 m (n=8) H_p: R^2=0.62 ε=0.582 m (n=26)	The model considers different illumination conditions. And the retrievals results of H_i are reasonable.	Retrievals results of H_p are more uncertain	Clear and overcast sky conditions	Spectrometers
König and Oppelt, 2020	Sea ice	The slope of the log-scaled spectrum at 710 nm and the solar zenith angle	H_p (H_p: 0–0.3 m)	R^2=0.79 ε=0.028 m (n=48)	Not affected by the characteristics of the underlying ice	The method is now only suitable for clear sky condition and cannot be used for H_i retrieving now	Clear sky condition	Spectrometers

2.1.1 Method of Legleiter et al.

Legleiter et al. (2014) retrieved Greenland glacier melt ponds depth based on the ratio of the reflectance of different bands. Due to the instruments being placed over sub-kilometer distances, the differences in solar zenith angle between the sensors were negligible. The reflectance R was obtained by multiplying the ratio of upwelling spectral radiance to downwelling spectral irradiance (R_{rs}) by π, because a Lambertian bidirectional reflectance distribution function was assumed. Under these conditions, reflectance R equals albedo.

The basic theory is that the total upwelling irradiance $F_T(\lambda)$ on the surface of a melt pond is the sum of contributions from the bottom, the water column, the water surface, and the atmosphere ($F_p(\lambda)$). Among these components, only the irradiance reflected from the pond bottom, $F_b(\lambda)$, is directly related to depth; it decreases exponentially with increasing H_p. Radiative transfer in the melt pond is mainly affected by the absorption coefficient k of the water. The long-wave irradiance $F_T(\lambda_2)$ attenuates faster than the short-wave irradiance $F_T(\lambda_1)$ ($\lambda_2>\lambda_1$, $k(\lambda_2)>k(\lambda_1)$, λ_2 and λ_1 represent different wavelengths). $F_T(\lambda_1)/F_T(\lambda_2)$ increases with greater H_p. Therefore, the upwelling irradiance ratio X of different bands can be used to express the influence of melt pond water depth on radiation attenuation. For the same incident irradiance, the ratio of upwelling irradiance at different bands can also be simplified as the ratio of albedo. Under reasonably good atmospheric conditions where H_p is tens of centimeters and the water is relatively clear, other irradiance components in the melt pond can be ignored (Legleiter et al. 2009). $F_T(\lambda)$ mainly depends on $F_b(\lambda)$. Furthermore, X and H_p are linearly related.

Using field observations to verify this theory, it was determined that when λ_1 = 584 nm, λ_2 = 599 nm, the correlation between X and H_p was the highest (R^2 = 0.94). And the correlation coefficient matrix also indicated that many other band combinations had R^2 values that were almost as high. Legleiter et al. (2014) convolved the field spectra to match the spectral response functions of the WorldView2 (WV2) satellite and found that the correlation was still high. Finally, to verify the feasibility of using satellite data to retrieve H_p, a correlation analysis was conducted between a randomly selected subset (50%) of H_p measured in the field and X obtained from WV2 satellite images, and the largest correlation coefficient between X and H_p was R^2 = 0.92. Using the other half of the observed data for verification, the correlation coefficient between the retrieved and the measured H_p was R^2 = 0.93 and ε = 0.65 m, which proved that this method could be used for the satellite to retrieve H_p.

2.1.2 Method of Lu et al.

Lu et al. (2018a) established a quantitative relationship between the color C of melt pond and both H_p and H_i. Color is an apparent optical property that is easy to observe. Physically, there is no distinct difference between color and albedo because both are quantities describing the reflected radiation by a surface. However, mathematically, color here refers to the values measured by a digital camera in the visible band. The value of a color consists of three intensity values in different bands: red, green, and blue.

In the Arctic summer, even on the same ice floe, the color of melt ponds varies greatly, depending largely on the nature of the water body and the underlying ice. The TEA model is used to calculate the albedo of the melt pond, by utilizing the colorimetric method that converts the reflection spectrum into the three RGB primary colors. Then, the relationship between H_i, H_p, and the color C can be established.

Melt pond color C is affected by pond depth, underlying ice thickness, the incident solar radiation level and optical properties of ice. The influences of H_i and H_p are the most important. So, pond color can be expressed as $C = f(H_i, H_p)$, where C is a vector composed of the intensities of red, green, and blue in the RGB color space or of hue, saturation, and brightness in the HSL (hue-saturation-luminance) color space. The C calculated by this model was consistent well with measured results (R^2 = 0.676), which proved the feasibility of the proposed method. This indicated the possibility of retrieving H_i and H_p from melt pond color, i.e., $(H_i, H_p) = f^1(C)$. The retrievals H_i and H_p of the inverse function were compared with the measured data. The relationship between simulated and measured H_i was not clear. So did for H_p. But a good agreement can be found for thin ice with H_i <1 m (R^2 = 0.671 and ε = 0.156 m).

2.1.3 Method of Malinka et al.

Malinka et al. (2018) showed that pond reflectance is mainly determined by the albedo of the underlying ice. The basic idea is based on radiation transfer theory. If the absorption and transport scattering coefficients of the underlying ice are known, then a two-stream approximation can be used to calculate the melt pond bottom albedo α_b (α_b=$f(\sigma_t, H_i)$, where σ_t is the transport scattering coefficient of under-pond ice, and the absorption coefficient of sea ice is equal to that of pure ice. The melt pond surface albedo α can be further calculated using α_b and H_p. Therefore, α is mainly determined by three parameters: H_p, σ_t, and H_i. For the illumination conditions, Malinka et al. (2018) considered both the direct and diffuse incident solar radiation. Clear sky conditions were influenced by the solar zenith angle, while for overcast conditions diffuse irradiance was assumed. For a mixture of direct and diffuse incidence, Malinka et al. (2018) confirmed the effect of the background was negligible, so the results of the melt pond albedo measurements can be processed without a prior knowledge of the albedo of the surrounding background. Melt ponds have a smaller and constant albedo contrast to white ice and snow for wavelengths longer than 0.9 μm.

Because snow and ice have a local maximum at about 1.1 μm. Thus, this slight peak can be considered as a criterion for determining if a spectrum is taken entirely from an open pond or partially from snow/ice surface. In the Arctic, most sky conditions were overcast in summer, so only a few measurements were taken at clear sky conditions. In the cases of overcast sky, the measured albedo was interpreted as the white-sky one. In the clear-sky cases, the Rayleigh atmosphere with the Arctic background aerosol was assumed. In this case the solar incidence angle was determined from the pond reflection in the infrared range (IR): at intervals of 1.25–1.3 μm (ideal) or 0.85–0.9 μm.

These three parameters, H_i, H_p, and σ_t, make up a 3-D vector, which was varied according to the Newton-Raphson method to provide the best fit (in the sense of least squares) of the measured and modeled spectra. Malinka et al. (2018) verified this model with different field observation data sets. The retrievals results of H_i were found to be essentially consistent with the measured value (R^2 = 0.56 and ε = 0.215 m). Due to the pond reflectance depends poorly on its water depth, the retrieval of the H_p is uncertain: its value can differ up to 2 times from the measured one (R^2 = 0.62 and ε = 0.582 m).

2.1.4 Method of König and Oppelt

The method proposed by König and Oppelt (2020) uses the spectral data of bare ice surfaces to simulate melt pond spectra for model development and validate the model with in situ melt pond measurements. The specific steps are to define a water column without absorption and scattering water constituents on bare ice and to calculate the reflectance of the water surface. The depth of the water column and the type of underlying ice can both vary, and finally a reflection spectrum library containing five different types of underlying ice and different melt pond depths between 0 and 100 cm can be generated. Based on this spectral library, the correlation between H_p and the slope of the log-scaled spectrum, $y(\lambda)$, was studied. It was found that the r between H_p and y was −1 when λ was in the range of 700–750 nm. Analysis of field observation data confirmed this conclusion, with the r of about −0.9 for field measurements of H_p and y in the vicinity of the λ=700 nm band. And the slope of the log-scaled spectrum at 710 nm was widely independent of the bottom albedo. Based on this correlation, the slope of the log-scaled spectrum at 710 nm of the pond surface can be used to establish a linear model: $H_\mathrm{p} = f(y(710\ \mathrm{nm}))$. The slope and intercept of the linear model is influenced by the solar zenith angle. Therefore, the inputs for this model were the slope of the log-scaled spectrum and solar zenith angle. The theoretical depth range of the retrieval was 0–100 cm. And the model is only suitable for clear sky conditions. A strong linear correlation (R^2=0.74 and ε=0.028 m) is shown in the comparing between the simulated H_p and measured H_p with solar zenith angles varies from 58.9° to 61°.

2.2 Evaluation for the four methods

To achieve the retrieval of H_p and to take summer sea-ice thickness into account at the same time, the four methods described above must be improved based on a comprehensive assessment. Method of Legleiter et al. (2014) demonstrated the feasibility of retrieving H_p through melt pond surface albedo in a specific band. The results could be matched with the observation band of the remote-sensing satellite to achieve large-scale observations and retrievals. Although the Arctic summer H_p and H_i were both less than those of glaciers, which increased the uncertainty and difficulty of retrieving H_p and H_i. However, the changes in the underlying ice caused changes in the surface reflection characteristics (Lu et al., 2016). So, this method is hoped to show changes in H_p and H_i by varying albedo.

Method of Lu et al. (2018a) show a good agreement when retrieving thin ice (H_i < 1 m) (R^2 = 0.671 and ε = 0.156 m), and a clear relationship between simulated and measured H_p is not shown. The retrieval H_i from method of Malinka et al. (2018) was reasonable (R^2 = 0.56 and ε = 0.215 m). But the H_p retrieval was uncertain (R^2 = 0.62 and ε = 0.582 m) and no improvement can be achieved unless additional information was used other than spectral reflectance in the visible range. The retrieval H_p from method of König and Oppelt (2020) requires a spectrum library based on field observation data, and the model is suitable for clear sky conditions. And cannot be used for retrieving H_i at its present state. The model is theoretically valid for the depth range of 0–100 cm and is influenced by solar zenith angle. In Figure 11 of König and Oppelt (2020), validations using field observations were conducted only within the depth range of 0–30 cm with sun zenith angles between 58.9° and 61°. To enlarge its validity range, more field data covering different weather and illumination conditions are necessary.

To sum up, we take the spectral albedo (350–1000 nm) into consideration and try to find two optimal bands for retrieving H_p and H_i according to Method of Legleiter et al. (2014). With more field data and more consideration of uncertain factors, e.g., the inherent optical properties (IOPs) of sea ice, the method could further reduce the uncertainty in retrievals. Therefore, it is theoretically feasible to separate the effects of H_p and H_i from the reflection characteristics.

2.3 Improvement and application of method

To find a general relationship between H_p and surface spectral albedo, two radiative transfer models are employed to implement the retrieval method of Legleiter et al. (2014). The estimated results of two models were used to build the retrieval method, then the field measurement data were used to verify the method. The TEA is a two-stream radiative transfer model which is under the assumptions of diffuse incident solar radiation and isotropic scattering. Assuming the continuity of radiation fluxes at the air-pond, pond-ice, and ice-ocean interfaces, the irradiance in both directions in each layer can be calculated as well as the melt-pond albedo α_λ. The model is governed by two coupled first-order differential equations (Lu et al., 2016):

$$\begin{cases} dF^{\downarrow}(z,\lambda) = -k_\lambda F^{\downarrow}(z,\lambda)dz - \sigma_\lambda F^{\downarrow}(z,\lambda)dz + \sigma_\lambda F^{\uparrow}(z,\lambda)dz \\ dF^{\uparrow}(z,\lambda) = -k_\lambda F^{\uparrow}(z,\lambda)dz + \sigma_\lambda F^{\uparrow}(z,\lambda)dz - \sigma_\lambda F^{\uparrow}(z,\lambda)dz \end{cases}, \quad (1)$$

where σ_λ is the wavelength-dependent scattering coefficient, and k_λ is the absorbing coefficient. $00(z, \lambda)$ are the upwelling and downwelling irradiances respectively. The BL model sub-divides the melt pond into two layers and the IOPs of each layer are constant.

In contrast with TEA, the BL model is also employed here. It also divides the underlying ice into one “drained layer (DL)” and four “interior layers (INT)”. The thickness of the DL and first INT is 1/4 of H_i. The thickness of each of the other three INT accounts for 1/4 of H_i each. The thickness of the DL is calculated based on the underlying ice thickness. When H_i <1.5m, the thickness of the DL is 1/30 of H_i; when H_i >1.5 m, the thickness of the DL is 0.05 m (Briegleb and Light, 2007). The radiative transfer equation for the BL model is:

$$\mu \frac{dF}{d\tau} + F = \frac{\omega}{4\pi}\int_{4\pi} d\Omega' S(\Omega,\Omega')F(\Omega',\tau) \quad , \quad (2)$$

where $\mu = \cos\theta$ is the incident angle, F is the irradiance, τ is the extinction optical depth when τ=0 at the layer upper boundary and $\tau = kz$ at the lower layer (z is the layer thickness), σ is the scattering coefficient ($\omega = \sigma/(\sigma+k)$), Ω and Ω' are the normalized direction vectors for the incoming and scattered beams, and $S=S(\Omega\Omega')$ is the scattering phase function.

To calculate radiative transfer in sea ice, certain parameters must be specified. The IOPs of sea ice and water have been fully discussed in Lu et al. (2016), and the results were used here. The absorption coefficient of sea ice and water of the two models can be got from Perovich (1996). Scattering in meltwater and ocean water is negligible. The scattering coefficient of sea ice is equal to 2.5 m^{-1} for TEA (Lu et al., 2016). For the BL model, due to the definition being different from that used in the TEA model, the scattering coefficient is 70 m^{-1} for DL, and 20 m^{-1} for INT. The asymmetry parameter of the BL model is 0.94 for sea ice (Briegleb and Light, 2007). Considering that the Arctic is mostly overcast sky condition during the summertime (Grenfell and Perovich, 2008). Therefore, both models used the incident solar irradiance measured by Grenfell and Perovich (2008) under a completely overcast sky conditions on August 7, 2005, with the solar disk not visible.

The specific steps of the improved retrieval method were as follows. (1) Based on the two models, the spectral albedo of the melt pond at an assumed depth (0–0.5 m) and underlying ice thickness (0.1–5 m) was calculated. (2) The r between H_p and $X(\lambda_1, \lambda_2) = ln[\alpha(\lambda_1)/\alpha(\lambda_2)]$ was then calculated to determine the retrieval equation $H_\mathrm{p} = f(X)$ corresponding to the maximum correlation coefficient and the wavelengths λ_1 and λ_2. (3) The theoretical retrieval models were then verified by field observations. This method was called the improved optical band ratio analysis (OBRA) method, and the retrieval method for H_i was similar. The two radiative transfer models were used to conduct theoretical calculations, to enable comparisons, and to increase the reliability of the results.

3 Results

3.1 Pond depth-spectral albedo relations

In this study, H_p was assumed to vary between 0 and 0.5 m, and H_i vary between 0.1 and 5 m. The range of ice thickness was slightly larger than the current state in the Arctic summer (Lang et al., 2017; Lu et al., 2018a). However, it was still beneficial to record the outcome of the proposed model under limited conditions. The improved OBRA method was used to calculate r between X (λ_1, λ_2) and H_p and Figure 1 shows the results. The selected waveband range was between 350 and 1000 nm, the main reasons are the strong interaction with water, ice, and snow, with 70%–80% of the solar energy reaching the Earth’s surface contained in this waveband (Liou 2002; Lu et al., 2016).

In respect to the results of the BL model, Fig. 1 shows that there were two situations in which X was strongly correlated with H_p. In the first situation, λ_1 was between 350 and 600 nm and λ_2 was between 600 and 800 nm; in the second situation, λ_1 was between 750 and 850 nm and λ_2 was between 850 and 1000 nm. The maximum r of 0.99 occurred when λ_1 = 359 nm and λ_2 = 605 nm. The TEA results were generally similar to those of the BL model. Corresponding bands of the maximum r were λ_1 = 350 nm and λ_2 = 611 nm. Moreover, in the two models, when λ_1 and λ_2 were both small or both large, or when λ_1 was small and λ_2 was large, the correlation between X and H_p was weak.

These results were due to the different IOPs of sea ice and pond water in the different bands. When λ_1 and λ_2 were small, the absorption capacity of sea ice and pond water was so weak that the solar radiation in this band passed through the melt pond, underlying ice, and reached the ocean easily. When both λ_1 and λ_2 were large, the incident radiance was easily absorbed by pond water. When λ_1 was small and λ_2 was large, the increase in H_p will result in a small change in the albedo of the shorter wavelength, but a large decrease in albedo at the longer wavelength due to strong absorption by melt pond water (Lu et al., 2018b). Whether the solar radiation passed through or was absorbed by the melt pond, it had a large effect on the upwelling irradiance reflected by the underlying ice, which in turn affects the upwelling irradiance on the surface of the melt pond. Therefore, the retrieval of H_p using the albedo of this band was not effective.

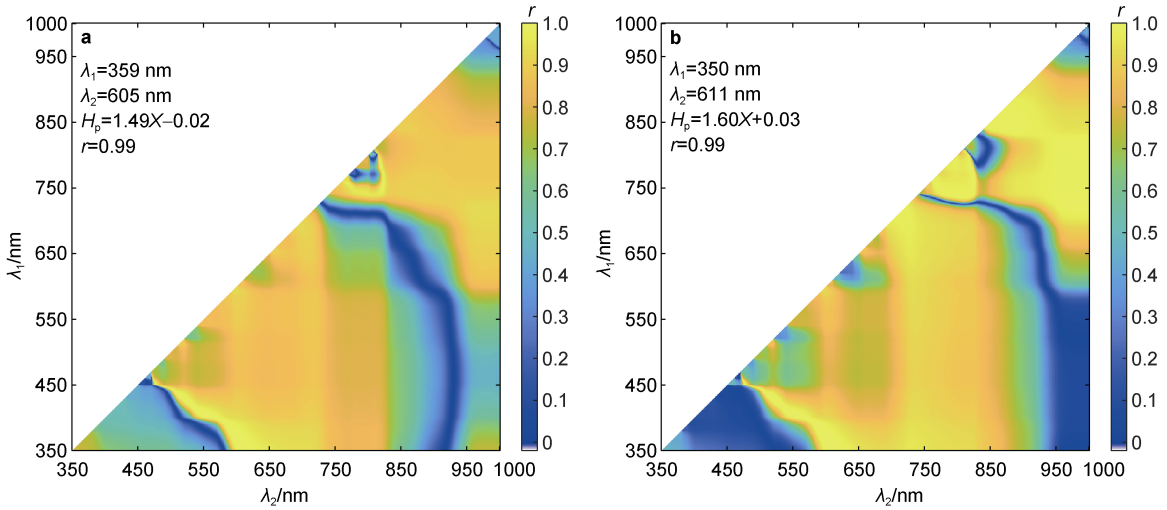

Figure 1 Correlation coefficients r between X (λ_1, λ_2) of the spectral albedo and H_p based on the BL model (**a**) and the TEA model (**b**). Also listed in the left corner are the information of best relations.

3.2 Verification of OBRA

Theoretical calculations revealed a strong correlation between X and H_p in a specific band. Table 2 summarizes the five different datasets of in situ field measurements that were used for the evaluation of the improved OBRA.

In these field data, part of the melt pond was covered by snow, which led to some points being deleted during the comparison due to the large difference between the actual conditions and the model. The other part of the melt pond was covered with ice, but when the ice lid was thin (2–3 cm), it had little impact on the albedo and transmittance of the melt pond (Lu et al., 2018c), and therefore the data could still be used for model verification. Perovich et al. (2002) carried out observations of a dual pond, and we compared the results with the findings of Malinka et al. (2018). This particular pond had a portion with a light bottom and a portion with a dark bottom. The water depth was the same in both sections, but the properties of the underlying ice differed. The ice in the lighter section had many more air bubbles than the ice in the darker section.

Table 2 Summary of the five different datasets used to evaluate the OBRA

Reference	location	Time	H_p	H_i	Sky condition
Cao et al. (2020)	Arctic	2018.7–2018.10	0–0.3 m	1–1.5 m	Overcast sky
Wang et al. (2018)	Arctic	2016.7–2016.10	0–0.3 m	0.5–1.0 m	Overcast sky
Istomina et al. (2016)	Arctic	2012.8–2012.10	0–0.5 m	0.4–3.0 m	Clear and overcast sky
Polashenski et al. (2012)	Barrow	2008–2009	0–0.3 m	–	Clear and overcast sky
Perovich et al. (2002a)	Beaufort Sea	1998.7–1998.8	–	0–1.2 m	Overcast sky

A comparison between H_p retrieved by the model and field-measured values under overcast sky conditions (Figure 2) showed that the range of H_p retrieved by the model was 0–0.4 m, which was consistent with the observed range. The correlation coefficient of the retrieval results from the BL model was $R^2 = 0.421$, at the significance level $P = 0.05$, the root-mean-squared error was $\varepsilon = 0.067$ m, and the average of the relative error $<\zeta> = 138\%$. The retrieval results of TEA had corresponding values of $R^2 = 0.426$, $P = 0.027$, $\varepsilon = 0.084$ m, and $<\zeta> = 228\%$. Most of the retrieval results of the BL and TEA models were within the range of $\pm 2\varepsilon$, namely the 95% confidence interval.

3.3 The influence of band selection

The above results showed that the spectral albedo of a specific wavelength can be used to retrieve H_p, and Figure 1 also shows that broader wavelength bands, rather than an essentially continuous spectrum, would be sufficient for H_p retrieval. To verify the feasibility of retrieving H_p over a wide band, satellite remote-sensing bands were further used to retrieve the depth of the Arctic melt pond. Different satellites had different bands and each type of satellite corresponds to a special situation was taken into consideration. As technology develops, more satellites and different satellite bands may become available. To obtain the general relationship, the wavelength width of the various bands of the MODIS and WV2 satellites was considered to be about 50 nm. The spectral albedo calculated previously was convolved with a step length of 50 nm, and the relationship between the ratio X^* of the

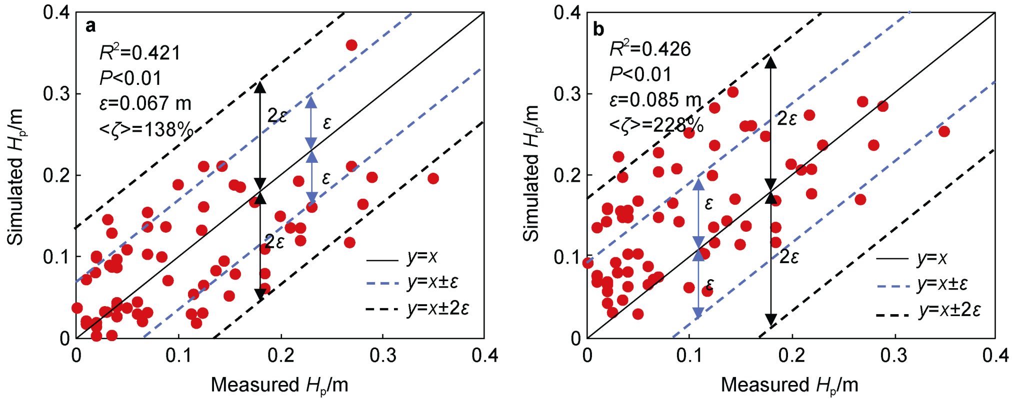

Figure 2 Comparison between the on-site measured H_p and the estimated values from the BL model (**a**), and the TEA model (**b**).

convolved albedo and H_p was recalculated. Figure 3 shows the results. Also supplied in the supporting material are results a step of 20 nm.

Figure 3 is similar to Figure 1, and further demonstrates the feasibility of using satellite-related wavebands to retrieve H_p. In the BL model results, the maximum correlation coefficient was found at a convolved albedo of λ^*_1 = 355–404 nm, λ^*_2 = 564–613 nm, which included the band with the largest correlation in the retrieval of spectral albedo. The TEA results resembled those of the BL model. Moreover, the two specific bands (λ^*_1, λ^*_2) of X^* calculated by the two models and the general relationships between X^* and H_p were similar, indicating that the field environment had a similar effect on the model when using the convolved albedo to retrieve H_p.

The theoretical calculations indicated a strong correlation between H_p and X^*. The field data for overcast sky conditions were convolved to verify the relationship; the results shown in Figure 4. The results retrieved from the BL and TEA models showed that the correlation coefficients between X^* and H_p were similar with the results between X and H_p, but ε and $<\zeta>$ are larger than that. Moreover, the retrieved H_p was greater than the measured. This phenomenon was much like the one that occurred when Legleiter et al. (2014) used the convolved spectrum to retrieve H_p and it could be explained in terms of adjacency effects. The reflectance of satellite remote sensing is located within a certain band and the step length of the convolved spectrum was close to the wavelength of the different satellite bands. This result was therefore beneficial for the use of satellite remote sensing to retrieve the depth of Arctic melt ponds. Regardless of whether the spectral albedo or convolved albedo was used to retrieve H_p, the corresponding wavelength band at the maximum correlation was within the visible light range. In the visible range of the MODIS satellite, the red band is 50 nm (620–670 nm), and the green (545–565 nm) and blue (459–479 nm) bands are both 20 nm. To further explore the feasibility of retrieving H_p by satellite remote sensing, the spectral albedo was convolved with a step length of 20 nm, and the relationship

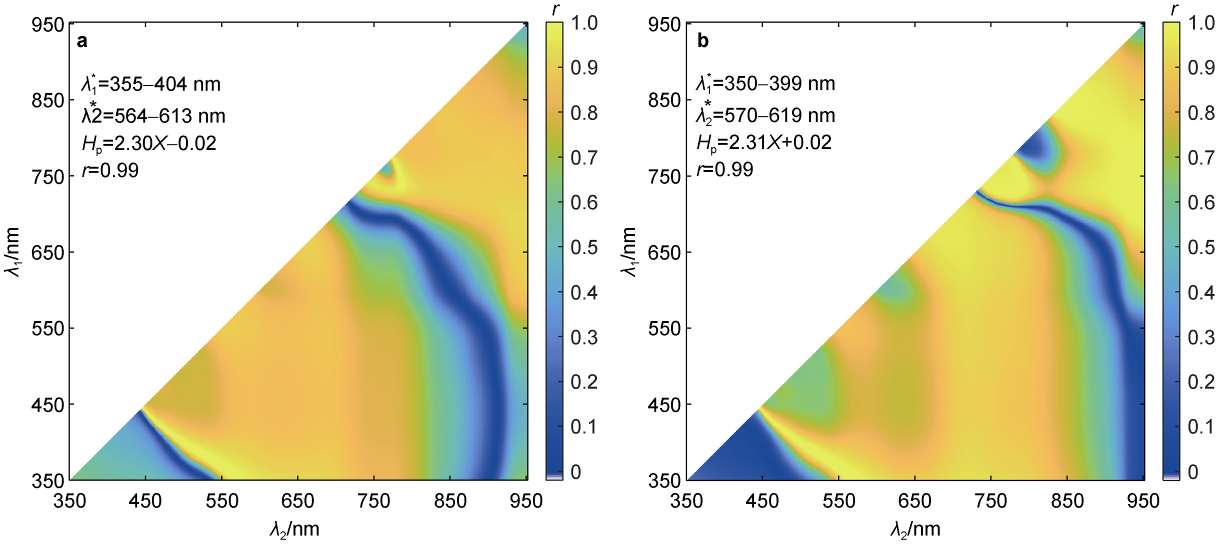

Figure 3 Correlation coefficient r between $X^*(\lambda^*_1, \lambda^*_2)$ of the convolved albedo and H_p based on the BL model (**a**) and the TEA model (**b**). Also listed in the left corner are the information of best relations.

between the ratio of convolved albedo $X^{*'}$ and H_p was estimated (see the attached material for the results). The ε and R^2 between the measured H_p and the simulated H_p resembled the results obtained from the convolved albedo with the 50-nm step. Under the maximum correlation coefficient, the corresponding band of the BL model was $\lambda^{*'}_1$ = 357–376 nm, $\lambda^{*'}_2$ = 591–610 nm, and that of TEA was $\lambda^{*'}_1$ = 350–369 nm, $\lambda^{*'}_2$ = 595–614 nm. The specific wavebands corresponding to the maximum correlation coefficients calculated by the two models were all within the range of λ^{*}_1 and λ^{*}_2 corresponding to the maximum correlation coefficient integrated by the 50-nm step. These results further proved the feasibility of the improved OBRA method for retrieving H_p using satellite remote sensing.

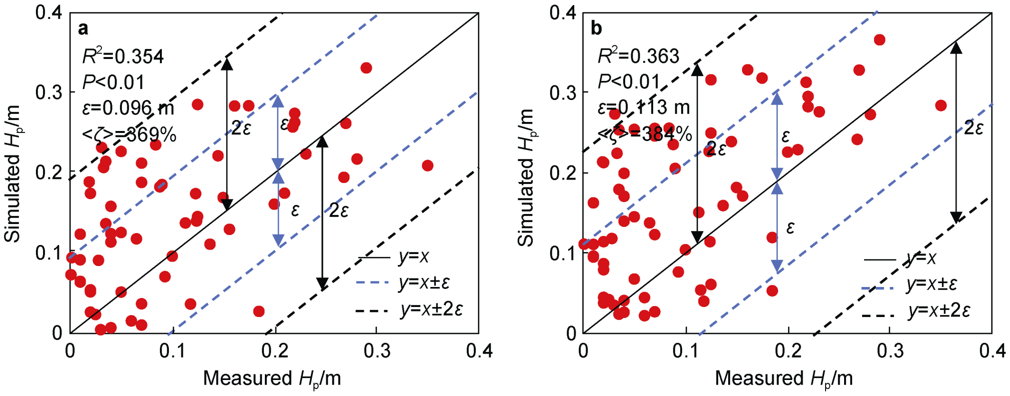

Figure 4 Comparison between the on-site measured H_p and the estimated values from the BL model (**a**), and the TEA mode l (**b**).

3.4 Underlying ice thickness-spectral albedo relations

The improved OBRA method can also be used to retrieve H_i. Figure 5 shows the correlation between X (λ_1, λ_2) and H_i. Figure 5 shows that the correlation between H_i and X was good only when λ_1 and λ_2 were both small (350–450 nm). This was because only the 350–450 nm solar irradiance band was likely to penetrate the melt pond and the sea ice to reach the subglacial ocean (Lu et al., 2018b), and then the characteristics of the underlying ice will affect the upwelling irradiance of this band on the surface of the melt pond. When retrieving H_i, the convolved albedo shown in Figure 3 was not used. This was because the uncertainty of retrieving H_i was great, and λ_1 and λ_2 were both small and relatively close at this time, resulting in the retrieval bands overlapping after convolution. On-site measured data for overcast sky conditions were further used to verify this relationship, the results of which were shown in Figure 6.

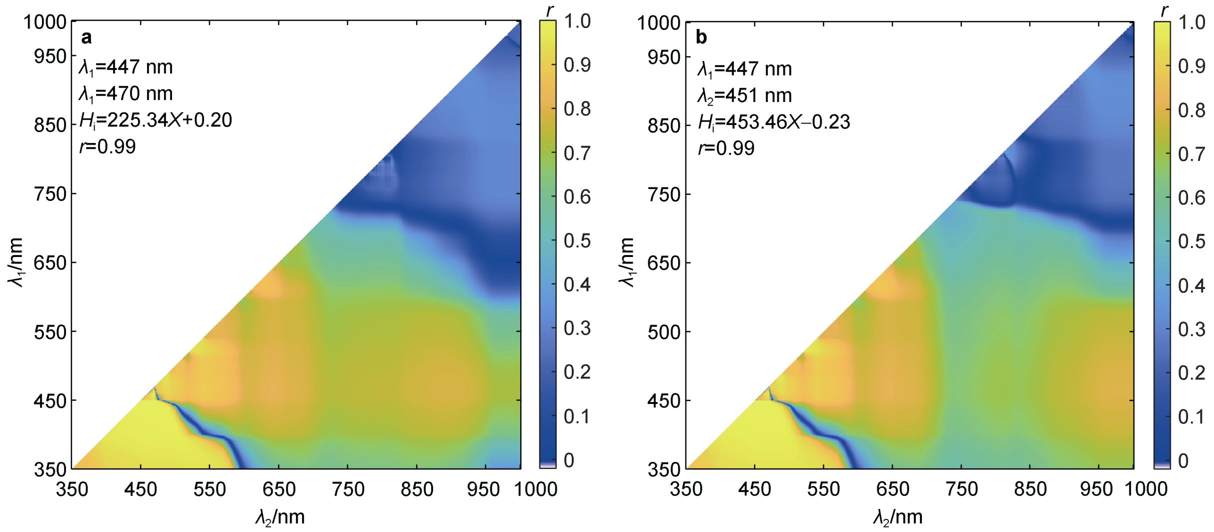

Figure 5 Correlation coefficient r between X (λ_1, λ_2) of the spectral albedo and H_i based onthe BL model (**a**) and the TEA model (**b**). Also listed in the left corner are the information of best relations

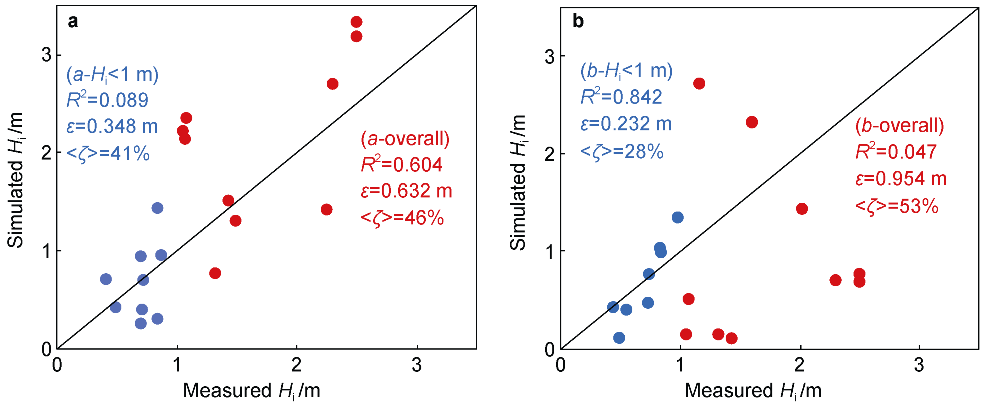

Figure 6 Comparison between the on-site measured H_i and the estimated values from the BL model (**a**), and the TEA model (**b**).

Comparison of H_i retrieved by the models and the on-site measured values revealed that H_i retrieved by the models was in the 0–3.5 m range, which was consistent with the observed range. The correlation coefficient between the measured and simulated H_i using the BL model was $R^2 = 0.604$, $\varepsilon = 0.632$ m, and $<\zeta> = 46\%$; while the overall relationship between simulated and measured H_i is not apparent for TEA ($R^2 = 0.047$, $\varepsilon = 0.954$ m and $<\zeta> = 53\%$).

But a good agreement can be found for thin ice with H_i <1 m for TEA. The correlation coefficient of the TEA between measured and simulated H_i was $R^2 = 0.842$, $\varepsilon = 0.232$ m and $<\zeta> = 28\%$. While the relationship from the BL model was not clear in the range of H_i <1 m ($R^2 = 0.089$, $\varepsilon = 0.348$ m and $<\zeta> = 41\%$). This indicated that the present retrieval method for TEA was more suitable for thin ice than thick ice.

Nevertheless, the results were still encouraging. Affected by global warming, the Arctic sea ice is undergoing a rapid melting process, and the sea ice is continuously thinning. Lindsay and Schweiger (2015) found that the declining trend in annual mean ice thickness over the Arctic Basin was -0.58 ± 0.07 m·decade^{-1} over the period of 1975–2012, with the annual mean ice thickness decreasing from 3.59 m in 1975 to 1.25 m in 2012. Namely, the range of H_i <1 m will be critical for Arctic summer sea ice retrievals. The results provided support for a possible new method of determining ice thickness, which would complement our understanding of summer sea-ice thickness.

4 Discussion

To assess the validity of the method under clear sky conditions, we used the BL model to calculate the spectral albedo of a melt pond under different illumination conditions by adjusting the ratio of direct (rdir) and diffuse incident irradiance (rdif) (rdir = 100%, rdif = 0%; rdir = 75%, rdif = 25%; …; rdir = 0%, rdif = 100%) at solar zenith angle of 60°. Following Lu et al. (2016), $H_p = 0.3$ m and $H_i = 1.0$ m were used, corresponding to a clear water pond on a typical Arctic FYI. The results are shown in Figure 7.

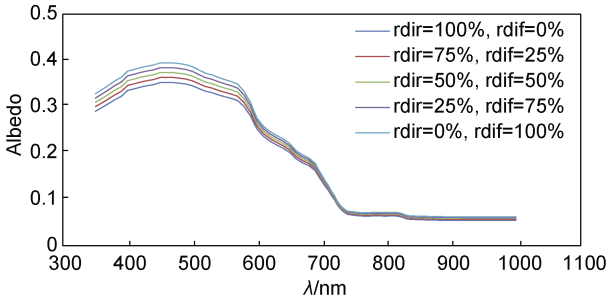

Figure 7 The influence of different sky conditions on albedo.

The differences among these spectral albedos were dependent on the ratio of rdir and rdif. As can be seen in Figure 7, the effects of sky conditions on the model can be neglected, and only small differences were seen. We applied the pond data under clear sky conditions to verify the relationship between H_p and X.

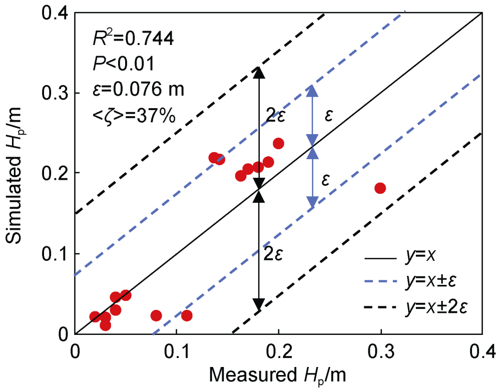

Figure 8 Comparison between the on-site measured H_p in clear sky and the estimated values from the BL model.

A clearer relationship was presented under clear sky condition than under overcast sky conditions. The correlation coefficient of the retrieval results of the BL model was $R^2 = 0.744$, $P = 0.01$, $\varepsilon = 0.0756$ m, and $<\zeta> = 37\%$. The main reason is that the OBRA method had a smaller $F_p(\lambda)$ under clear sky condition than under overcast sky conditions (Legleiter et al., 2009). The smaller the $F_p(\lambda)$ is, the smaller the model error is when it is ignored. At present, only limited data are available on Arctic sea ice under melt ponds during summer. More validations from field observations are required to verify the model under clear sky condition.

Besides, the original method was used for glaciers, which have an infinite optical depth and quite stable optical properties, while sea ice is much thinner and has much less air bubbles, causing strong uncertainty in its albedo. At the same time, the inherent optical properties of first- or multi-year ice can be different. But there is not much research that can be referred to, so we set the IOPs of ice as constant. This may be a factor limiting the accuracy of the model. To improve the accuracy, more field data and studies of sea ice IOPs are necessary.

5 Conclusions

This paper summarized the four methods of retrieving H_p and H_i proposed in recent years. Based on an improvement of the method from Legleiter et al. (2014), we established a general relationship between pond depth, underlying ice thickness, and spectral albedo using BL and TEA models, and provided a feasible method to retrieve H_p and H_i at the same time.

Five key results were obtained. (1) There was a strong correlation ($r = 0.99$) between X and H_p as well as that between X and H_i. (2) When retrieving H_p using the convolved spectrum, the correlation coefficient ($R^2 = 0.354$ for the BL model) was lower than that obtained using the continuous spectrum ($R^2 = 0.421$ for the BL model) due to the adjacency effect. The same was observed for the TEA model. (3) Different illumination conditions had a large influence on the performance of the improved OBRA. Clear sky conditions reduced the irradiance reflected by the atmosphere and improved the accuracy ($R^2 = 0.744$). (4) Due to the differences in model settings and field conditions, the application of the BL and TEA models had a certain influence on the retrieval results, which could also be used to compare with and verify each other. When the spectral albedo and convolved albedo were used to retrieve H_p, the results of the two models were quite similar. When retrieving H_i using the spectral albedo, the results for the BL model were suitable for the overall relationship ($0< H_i < 3.5$ m, $R^2 = 0.632$), while the TEA model was only applicable for thin ice retrieval ($H_i <1$ m, $R^2 = 0.842$). (5) The BL model was more complex than TEA and it satisfied the anisotropy assumption. TEA satisfied the isotropy assumption, was easier to calculate, had an analytical solution and could do more analysis. When the differences between the two models were not large, we can use a brief model.

It is anticipated that, using the improved method, spectral albedo can be used to retrieve H_p and H_i. And this method is not only can be used in field observations but also in remote sensing. Information about changes in melt pond depth and underlying ice thickness is helpful to improve our understanding of the entire melting process of Arctic melt ponds and their impacts on climate change.

Acknowledgement This research was supported by the National Key R&D Program of China (Grant no. 2018YFA0605901), the National Natural Science Foundation of China (Grant nos. 41922045, 41676187). We would like to thank the two anonymous reviewers and Associate Editor, Dr. Jon Ove Hagen for their valuable suggestions and comments regarding further improvement of this article.

References

Briegleb B P, Light B. 2007. A Delta-Eddington multiple scattering parameterization for solar radiation in the sea ice component of the Community Climate System Model. NCAR Tech. Note TN-4721STR.

Cao X W, Lu P, Lei R B, et al. 2020. Physical and optical characteristics of sea ice in the Pacific Arctic Sector during the summer of 2018. Acta Oceanol Sin, 39(9): 25-37, doi:10.1007/s13131-020-1645-6.

Farrell S L, Duncan K, Buckley E M, et al. 2020. Mapping sea ice surface topography in high fidelity with ICESat-2. Geophys Res Lett, 47(21): e2020GL090708, doi:10.1029/2020GL090708.

Grenfell T C, Perovich D K. 2008. Incident spectral irradiance in the Arctic Basin during the summer and fall. J Geophys Res: Atmos, 113(D12): D12117, doi:10.1029/2007JD009418.

Holland M M, Bitz C M, Tremblay B. 2006. Future abrupt reductions in the summer Arctic sea ice. Geophys Res Lett, 33(23): L23503, doi: 10.1029/2006GL028024.

Istomina L, Nicolaus M, Perovich D K. 2016. Surface spectral albedo complementary to ROV transmittance measurements at 6 ice stations during Polarstern Cruise ARK-XXⅧ/3 (IceArc) in 2012, doi: 10.1594/PANGAEA.867292.

Ji Q. 2015. Study on spatial-temporal change of Arctic sea ice thickness based on satellite altimetry. Wuhan University, PhD dissertation.

Ji Q, Pang X P, Zhao X, et al. 2015. Comparison of sea ice thickness retrieval algorithms from CryoSat-2 satellite altimeter data. Geomat Inf Sci Wuhan Univ, 40(11): 1467-1472, doi:10.13203/j.whugis20150279 (in Chinese with English abstract).

Katlein C, Arndt S, Nicolaus M, et al. 2015. Influence of ice thickness and surface properties on light transmission through Arctic sea ice. J Geophys Res: Oceans, 120(9): 5932-5944, doi:10.1002/2015JC010914.

König M, Oppelt N. 2020. A linear model to derive melt pond depth on Arctic sea ice from hyperspectral data. The Cryosphere, 14(8): 2567-2579, doi:10.5194/tc-14-2567-2020.

Kwok R, Cunningham G F. 2008. ICESat over Arctic sea ice: Estimation of snow depth and ice thickness. J Geophys Res: Oceans, 113(C8): C08010, doi:10.1029/2008JC004753.

Kwok R, Rothrock D A. 2009. Decline in Arctic sea ice thickness from submarine and ICESat records: 1958-2008. Geophys Res Lett, 36(15): L15501, doi:10.1029/2009GL039035.

Lang A, Yang S T, Kaas E. 2017. Sea ice thickness and recent Arctic warming. Geophys Res Lett, 44(1): 409-418, doi:10.1002/2016GL071274.

Legleiter C J, Roberts D A, Lawrence R L. 2009. Spectrally based remote sensing of river bathymetry. Earth Surf Process Landf, 34(8): 1039-1059, doi:10.1002/esp.1787.

Legleiter C J, Tedesco M, Smith L C, et al. 2014. Mapping the bathymetry of supraglacial lakes and streams on the Greenland Ice Sheet using field measurements and high-resolution satellite images. The Cryosphere, 8(1): 215-228, doi: 10.5194/tc-8-215-2014.

Lenton M L. 2012. Arctic climate tipping points. AMBIO, 41(1): 10-22, doi: 10.1007/sl3280-011-0221-x.

Li L Y, Ke C Q, Xie H J, et al. 2017. Aerial observations of sea ice and melt ponds near the North Pole during CHINARE2010. Acta Oceanol Sin, 36(1): 64-72, doi:10.1007/s13131-017-0994-2.

Lindsay R and Schweiger A. 2015. Arctic sea ice thickness loss determined using subsurface, aircraft, and satellite observatiobs. The Cryosphere, 9(1): 269-283, doi: 10.5194/tc-9-269-2015.

Liou K N. 2002. An introduction to atmosphere radiation, doi: 10.1088/0031-9112/32/6/041.

Lu P, Leppäranta M, Cheng B, et al. 2016. Influence of melt-pond depth and ice thickness on Arctic sea-ice albedo and light transmittance. Cold Reg Sci Technol, 124: 1-10, doi:10.1016/ j.coldregions. 2015.12.010.

Lu P, Leppäranta M, Cheng B, et al. 2018a. The color of melt ponds on Arctic sea ice. The Cryosphere, 12(4): 1331-1345, doi: 10.5194/tc-12-1331-2018.

Lu P, Cheng B, Leppäranta M, et al. 2018b. Partitioning of solar radiation in Arctic sea ice during melt season. Oceanologia, 60(4): 464-477, doi: 10.1016/j.oceano.2018.03.002.

Lu P, Cao X, Wang Q, et al. 2018c. Impact of a surface ice lid on the optical properties of melt ponds. J Geophys Res: Oceans, 123(11): 8313-8328, doi:10.1029/2018JC014161.

Makshtas A P, Podgorny I A. 1996. Calculation of melt pond albedos on Arctic sea ice. Polar Res, 15(1): 43-52, doi:10.1111/j.1751-8369.1996.tb00457.x.

Malinka A, Zege E, Istomina L, et al. 2018. Reflective properties of melt ponds on sea ice. The Cryosphere, 12(6): 1921-1937, doi: 10.5194/tc-12-1921-2018.

Notz D, Worster M G. 2009. Desalination processes of sea ice revisited. J Geophys Res: Oceans, 114(C5): C05006, doi:10.1029/2008JC004885.

Perovich D K. 1996. The optical properties of sea ice. Cold Regions Research and Engineering Laboratory.

Perovich D K, Grenfell T C, Light B, et al. 2002a. Seasonal evolution of the albedo of multiyear Arctic sea ice. J Geophys Res: Oceans, 107(C10): SHE20-1, doi:10.1029/2000JC000438.

Perovich D K, Tucker III W B, Ligett K A. 2002b. Aerial observations of the evolution of ice surface conditions during summer. J Geophys Res: Oceans, 107(C10): SHE24-1, doi:10.1029/2000JC000449.

Perovich D K, Grenfell T C, Richter-Menge J A, et al. 2003. Thin and thinner: Sea ice mass balance measurements during SHEBA. J Geophys Res: Oceans, 108(C3): 8050, doi:10.1029/2001JC001079.

Polashenski C, Perovich D, Courville Z. 2012. The mechanisms of sea ice melt pond formation and evolution. J Geophys Res: Oceans, 117(C1): C01001, doi:10.1029/2011JC007231.

Popović P, Abbot D. 2017. A simple model for the evolution of melt pond coverage on permeable Arctic sea ice. The Cryosphere, 11(3): 1149-1172, doi: 10.5194/tc-11-1149-2017.

Qin D, Zhou B, Xiao C. 2014. Progress in studies of cryosphere change and their impacts on climate of China. Acta Meteorol Sin, 72(5): 869-879, doi: 10.11676/qxxb2014.080.

Scott F, Feltham D L. 2010. A model of the three-dimensional evolution of Arctic melt ponds on first-year and multiyear sea ice. J Geophys Res: Oceans, 115(C12): C12064, doi:10.1029/2010JC006156.

Skyllingstad E D, Paulson C A, Perovich D K. 2009. Simulation of melt pond evolution on level ice. J Geophys Res: Oceans, 114(C12): C12019, doi:10.1029/2009JC005363.

Stroeve J, Holland M M, Meier W, et al. 2007. Arctic sea ice decline: faster than forecast. Geophys Res Lett, 34(9): L09501, doi:10.1029/2007GL029703.

Tsamados M, Feltham D, Petty A, et al. 2015. Processes controlling surface, bottom and lateral melt of Arctic sea ice in a state of the art sea ice model. Phil Trans R Soc A: Mathematical, Physical and Engineering Sciences, 373(2052): 20140167, doi: 10.1098/rsta. 2014.0167.

Wang M F, Su J, Landy J, et al. 2020. A new algorithm for sea ice melt pond fraction estimation from high-resolution optical satellite imagery. J Geophys Res: Oceans, 125(10): e2019JC015716, doi:10.1029/2019JC015716.

Wang Q K, Li Z J, Lu P, et al. 2018. 2014 summer Arctic sea ice thickness and concentration from shipborne observations. Int J Digit Earth, 12(8): 931-947, doi:10.1080/17538947.2017.1421720.

Supplementary Material

This is an auxiliary note for "Retrievals of Arctic sea ice melt pond depth and underlying ice thickness using optical data".

To further explore the feasibility of retrieving melt pond depth by satellite remote sensing, the estimated spectral albedo was convolved with a step length of 20 nm, and the relationship between the ratio of convolved albedo $X^{*'}$ and H_p was shown in Supplementary Figure A.

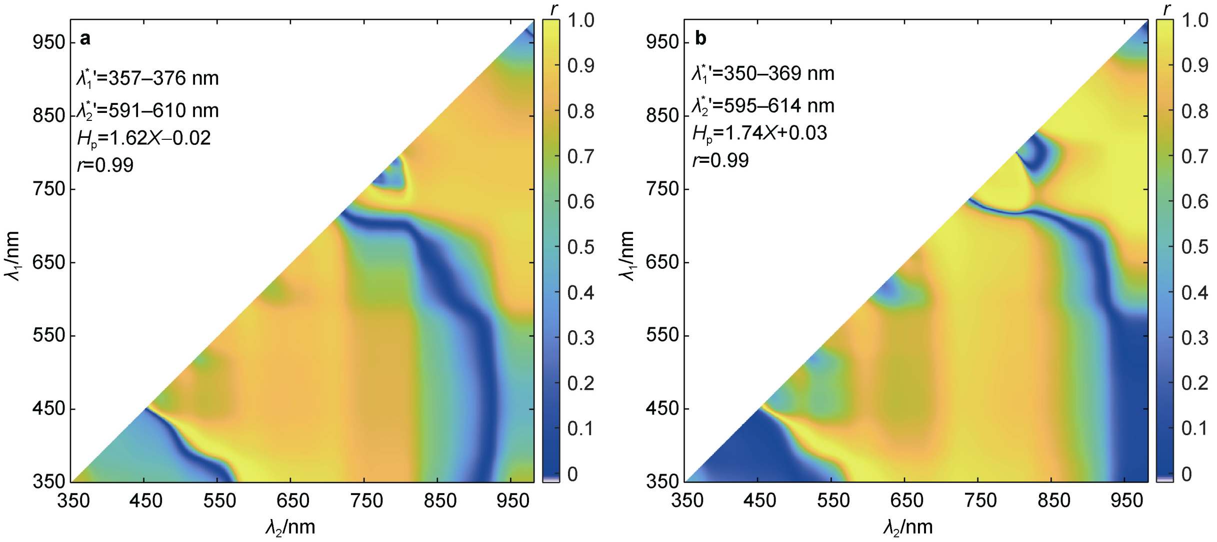

Supplementary Figure A Correlation coefficient r between $X^{*'}(\lambda^{*'}_1, \lambda^{*'}_2)$ and H_p based on the BL model (**a**) and the TEA model (**b**). Also listed in the left corner are the information of best relations

In the estimated results of the BL model, the maximum correlation coefficient was found at a convolved albedo of $\lambda^{*'}_1$=357–376 nm, $\lambda^{*'}_2$=591–610 nm, which covered the band with the largest correlation in the retrieval of spectral albedo.

The $\lambda^{*'}_1$ and $\lambda^{*'}_2$ corresponding to the maximum r calculated by the two models were all within the range of λ^{*}_1 and λ^{*}_2. The estimated results of TEA were much like those of the BL model.

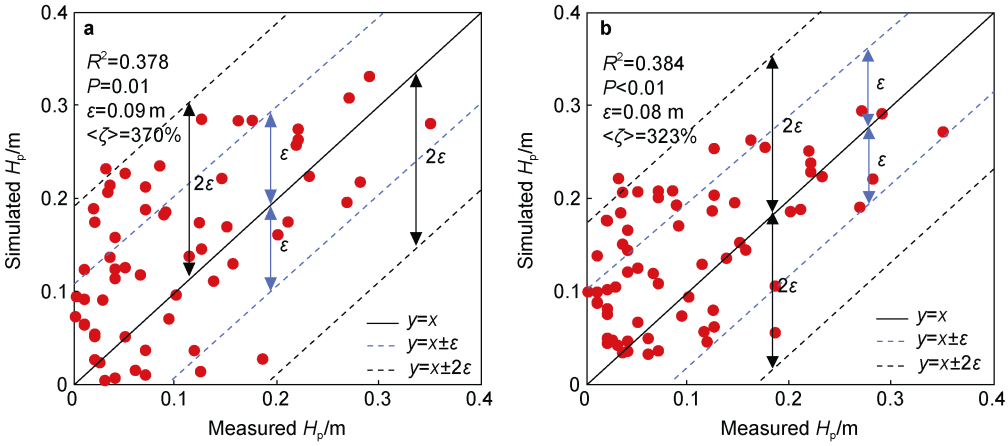

Supplementary Figure B Comparison between the on-site measured H_p and the estimated values from the BL model (**a**), and the TEA model (**b**).

The calculations showed a strong correlation between H_p and $X^{*'}$ in a specific convolved band. The field data under overcast sky conditions was convolved to verify the relationship. The results shown in Supplementary Figure B were quite similar to that of convolved albedo with 50 nm.

Supplementary Table A Abbreviations

Abbreviation	Full name
BL model	Delta-Eddington model
C	Melt pond color
DL	Drained layer for the BL model
$F_o(\lambda)$	Incident solar irradiance
$F_T(\lambda)$	The total upwelling irradiance on the surface of a melt pond
$F_p(\lambda)$	Path irradiance from the atmosphere
$F_b(\lambda)$	Bottom-reflected irradiance
$F^{\uparrow}(z, \lambda)$, $F_{\downarrow}(z, \lambda)$	The upwelling and downwelling irradiance
HSL	Hue, Saturation, Lumination
INT	Interior layer for the BL model
k	The absorption coefficient of pond water
n	The number of samples used for verification
P	The significance level
r	The Pearson's correlation coefficient
R^2	Correlation coefficient
RGB	Red, Green, Blue
$S=S(\Omega\Omega')$	Scattering phase function
X	The ratio of spectral melt-pond albedo in two bands
X^*	The ratio of convolved albedo in 50-nm
$X^{*'}$	The ratio of convolved albedo in 20-nm
$y(\lambda)$	The slope of the log-scaled spectrum
z	The layer thickness
$\alpha(\lambda)$	The spectral albedo of the melt pond
$\alpha_b(\lambda)$	The albedo of the bottom of the melt pond
σ_t	The scattering coefficient of under-pond ice
$\mu=\cos\theta$	Cosine the zenith angle
τ	The optical depth
σ	The scattering coefficient
λ	Wavelength
$<\zeta>$	The average of the relative error
ε	Root mean square error